Biophysical Journal
Article

Biophysical Society

ATP:Mg^{2+} shapes material properties of protein-RNA condensates and their partitioning of clients

N. Amy Yewdall,[1,*] Alain A. M. André,[1] Merlijn H. I. van Haren,[1] Frank H. T. Nelissen,[1] Aafke Jonker,[1] and Evan Spruijt[1,*]
[1]Institute for Molecules and Materials, Radboud University, Nijmegen, the Netherlands

ABSTRACT Many cellular condensates are heterotypic mixtures of proteins and RNA formed in complex environments. Magnesium ions (Mg^{2+}) and ATP can impact RNA folding, and local intracellular levels of these factors can vary significantly. However, the effect of ATP:Mg^{2+} on the material properties of protein-RNA condensates is largely unknown. Here, we use an in vitro condensate model of nucleoli, made from nucleophosmin 1 (NPM1) proteins and ribosomal RNA (rRNA), to study the effect of ATP:Mg^{2+}. While NPM1 dynamics remain unchanged at increasing Mg^{2+} concentrations, the internal RNA dynamics dramatically slowed until a critical point, where gel-like states appeared, suggesting the RNA component alone forms a viscoelastic network that undergoes maturation driven by weak multivalent interactions. ATP reverses this arrest and liquefies the gel-like structures. ATP:Mg^{2+} also influenced the NPM1-rRNA composition of condensates and enhanced the partitioning of two clients: an arginine-rich peptide and a small nuclear RNA. By contrast, larger ribosome partitioning shows dependence on ATP:Mg^{2+} and can become reversibly trapped around NPM1-rRNA condensates. Lastly, we show that dissipative enzymatic reactions that deplete ATP can be used to control the shape, composition, and function of condensates. Our results illustrate how intracellular environments may regulate the state and client partitioning of RNA-containing condensates.

SIGNIFICANCE Heterotypic condensates made from protein and RNA, such as the nucleolus, can exhibit puzzling gel-like morphologies that are at odds with fast protein dynamics that suggest liquid-like properties. Here, we highlight the importance of the RNA component. We show that the protein-RNA condensates are dynamic, adapting to local ATP concentrations through Mg^{2+}-induced compaction of the RNA via enhanced RNA-RNA interactions and reversible RNA relaxation when ATP binds Mg^{2+} again. This, and our observation that the RNA component exhibits temperature-dependent aging, suggests the RNA component imparts viscoelastic properties onto protein-RNA condensates, driven by multivalent RNA-RNA interactions. In contrast, the protein component is free to diffuse throughout the RNA network. Other condensates containing RNA probably respond in similar ways to Mg^{2+} and ATP.

INTRODUCTION

Biomolecular condensates facilitate the spatiotemporal organization of cellular processes. Most biomolecular condensates are heterotypic, and many arise from mixtures of proteins and nucleic acids, such as RNA (1). Forming and existing in complex intracellular environments, the membraneless nature of condensates exposes them to local environmental fluctuations. These fluctuating factors—ions, small molecules, and temperature—can all regulate the molecular interactions within condensates, which, in turn, shape their biophysical properties to influence morphology and function (2,3). However, the intracellular parameter space of organisms is complex, variable, and not fully mapped. Therefore, in vitro studies can establish valuable insights into the influence of such factors on condensate form and function.

It is well established that RNA structure is strongly influenced by magnesium ion (Mg^{2+}) concentrations (1,4,5), which can range from 0.5–1 mM in eukaryotic cells and 1–5 mM in bacterial cells, as well as having an astounding in vivo metabolite-bound concentration range of 20–100 mM (4,6). Indeed, the free Mg^{2+} concentrations can vary throughout the cell cycle due to changes in levels of ATP, a nucleotide that strongly complexes Mg^{2+} (5,7,8). Despite this, there has so far been no systematic analysis of the effect of Mg^{2+} and ATP on shaping protein-RNA condensates.

Submitted April 5, 2022, and accepted for publication August 19, 2022.
*Correspondence: amy.yewdall@ru.nl or e.spruijt@science.ru.nl
Editor: Tuomas Knowles.
https://doi.org/10.1016/j.bpj.2022.08.025

With this, we are inspired by the nucleolus, a protein-RNA condensate that emerges during the eukaryotic interphase within a complex cellular environment. As the site of ribosome biogenesis, ribosomal RNA (rRNA) and various RNA-binding proteins are predominantly found in this dynamic, but highly viscous condensate. In vivo nucleoli have slow fusion timescales of ~30 min and nonspherical shapes (9–11), which are not well represented by in vitro models, that are often liquid-like. Other heterotypic biomolecular condensates show similar divergent dynamics between protein and RNA components (12). We hypothesize that RNA structuring and network formation, governed by Mg^{2+} and other environmental factors, can partly explain these differences and shape the viscoelastic material properties of in vitro models of protein-RNA condensates.

In this work, we approximate a part of the nucleolus by making model condensates from nucleophosmin 1 (NPM1) protein and rRNA. By altering Mg^{2+} in the environment of model protein-RNA condensates, we shed light on how this common divalent cation can dramatically slowed RNA diffusion dynamics until it arrested, and nonspherical condensate morphologies were observed. Additionally, NPM1-rRNA condensates underwent temperature-dependent aging, particularly the rRNA component, which further supports the hypothesis that condensate maturation is governed by multivalent RNA-RNA interactions, suggesting RNA's role in imparting viscoelastic material properties to the condensate as a whole. The Mg^{2+}-stabilized arrested rRNA gel-like condensates liquefied by either temperature or ATP concentration increase, with morphologies becoming increasingly spherical, and these changes reflected in more fluid rRNA dynamics. We probed the functional consequence of different ATP:Mg^{2+} on NPM1-rRNA condensates and showed that these small molecules can impact client molecule partitioning. In particular, we explored the intriguing formation of a 70S ribosome halo that transiently associated with the NPM1-rRNA condensates. To allude to the intracellular enzymatic control of ATP levels, we used a dissipative enzymatic reaction that depletes ATP to regulate the biophysical properties of in vitro condensates and the partitioning of ribosomes. Together, our results not only provide a useful perspective for interpreting in vivo observations but also show that protein-RNA condensates are highly responsive to their environment, with the environment affecting condensate properties, form, and function.

MATERIAL AND METHODS

Reagents

Unless otherwise stated, all materials were obtained from Sigma-Aldrich (St. Louis, MO, USA).

Cloning of NPM1-wild-type (WT) into pET28a plasmid

The human NPM1 gene was extracted from the pET28a(+)-NPM1-EGFP construct (gifted from R.K.) and cloned into a pET28a(+) vector using *NdeI* and *XhoI* restriction sites. The correct insertion was confirmed by sequencing (BaseClear, Leiden, the Netherlands), and this construct was called pET28a(+)-NPM1-WT.

NPM1 protein expression and purification

E. coli BL21 (DE3) was transformed with pET28a(+)-NPM1-WT. Overnight cultures were used to inoculate large flasks of Luria-Bertani media, then cells were grown at 37°C to an $OD_{600} = 0.5–0.7$, before protein expression was induced with 1 mM IPTG. Protein expression was carried out at 20°C for at least 16 h, after which the cells were harvested by centrifugation. The pellet was resuspended in lysis buffer (20 mM Tris-HCl [pH 7.5], 300 mM NaCl, 2 mM β-mercaptoethanol, 25 mM imidazole) containing 500 U Bezonase Nuclease and Bovine Pancreas RNAse A (VWR, Radnor, PA, USA). The resuspended cells were lysed using a homogenizer. Lysed samples were left at 4°C for 1 h to allow the enzymes to degrade the nucleic acids. The lysate was spun at 35,000 × *g* for 30 min at 4°C in a Beckman JA25.50 rotor. The clarified supernatant was loaded onto a 5 mL HisTrapFF (Cytiva, Marlborough, MA, USA). After loading, the column was washed with 50 mL lysis buffer, and the His-tagged NPM1 proteins were eluted using elution buffer (20 mM Tris-HCl [pH 7.5], 300 mM NaCl, 2 mM β-mercaptoethanol, 250 mM imidazole). Eluted proteins were concentrated to <5 mL and loaded onto a Superdex 200 16/600 (GE Healthcare, Chicago, IL, USA) size-exclusion column connected to an AKTA Basic FPLC (GE Healthcare) and preequilibrated in storage buffer (20 mM Tris-HCl [pH 7.5], 300 mM NaCl). Fractionation of proteins was carried out at 1 mL/min and monitored at 280 and 260 nm. The fractions of the main peak were pooled, and the protein concentration was determined using the NanoDrop One^{C} (Thermo Fisher Scientific, Waltham, MA, USA). If the resulting UV spectrum had a 260/280 ratio of >0.6, the protein sample was further purified using anion-exchange chromatography to remove contaminating nucleic acids. All protein isolates were dialyzed into storage buffer, aliquoted, snap frozen in liquid nitrogen, and stored at −80°C.

Protein labeling

The purified NPM1 proteins were labeled using AlexaFluor488 C_5 maleimide (Thermo Fisher Scientific) based on a previously published protocol (13). Excess dye was removed using anion exchange, and the protein dialyzed into storage buffer. The final protein concentration was determined using the NanoDrop One^{C}. A labeled NPM1 stock was mixed with unlabeled protein at a 1:9 ratio of labeled:unlabeled protein, and this mixture was called NPM1-A488.

Sucrose gradient purified *E. coli* BL21 70S ribosomes were labeled using either ATTO488 NHS-ester (ATTO-TEC, Siegen, Germany) or Dylight650 NHS-ester (Thermo Fisher Scientific) dyes, as previously reported (14). The purified and labeled ribosomes were stored in aliquots at −80°C until use. The final concentration of labeled 70S ribosome was estimated to be 5.1 (A488 for ATTO488-labeled ribosomes) and 6.3 μM (D650 for Dylight650-labeled ribosomes) determined using a Nanodrop 1000 (Isogen Life Science, Utrecht, the Netherlands).

E. coli rRNA purification

E. coli BL21 cells were harvested from a 1 L culture in Luria-Bertani media ($A_{600} = 1.5$), and the cells were washed twice in buffer A (50 mM Tris [pH 7.7], 60 mM potassium glutamate, 14 mM magnesium glutamate, 2 mM DTT). Washed cells were lysed using the homogenizer, and insoluble debris was spun down at 20,000 × *g* for 25 min. The supernatant containing the ribosomes was removed, and the ribosomes were pelleted by centrifugation for 3 h at 50,000 Rpm at 4°C in a Beckman Ti70.1 rotor. The pellet containing the ribosomes was resuspended in buffer A, and the rRNA was purified using standard phenol-chloroform extraction protocols. The final rRNA concentration was determined using the Nanodrop One^{C}, where 1 $OD_{260} = 40$ μg/mL RNA.

RNA labeling using periodate oxidation

The 3′ hydroxyl of RNA was labeled with AlexaFluor647-hydrazide (Thermo Fisher Scientific) using periodate oxidation based on manufacturer's protocol. The RNAs labeled using this procedure included the purified rRNA, polyadenylic acid potassium salt (P9403 Sigma), or polyuridylic acid potassium salt (P9528 Sigma). The nucleic acids were purified using a standard isopropanol precipitation followed by 70% ethanol precipitation or using the Amicon-Ultra spin concentrators (Millipore, Burlington, MA, USA) (as per method described (15)). An agarose gel was used to double check complete free dye removal, before the sample concentrations were calculated using the Nanodrop One^{C}, where 1 OD_{260} = 40 μg/mL RNA, and the dye fluorescence concentration was calculated using the extinction coefficient (at 649 nm) of 250,000 $cm^{-1}M^{-1}$ (as described by the manufacturer). The AlexaFluor647-labeled RNAs were denoted with A647.

Making NPM1-RNA condensates

All experiments were performed using a standard base buffer (20 mM Tris-HCl [pH 7.2], 250 mM potassium glutamate) with different concentrations of magnesium glutamate (often denoted as Mg^{2+}), as specified per experiment. The buffers were made as a 4× concentrated stock and were diluted to a final 1× working concentration, along with the other components, using Milli-Q water. The final concentrations of NPM1 protein and RNA used in every experiment were 20 μM and 100 ng/μL, respectively. Under all buffer conditions, NPM1 was required to nucleate NPM1-RNA condensate formation. In a typical experiment, the 4× buffer is first mixed with Milli-Q water, followed by RNA, then the NPM1, after which samples were mixed and pipetted onto a functionalized microscopy slide for imaging. Unless otherwise stated, samples were left to incubate on the glass slides at room temperature for at least 45 min before imaging.

Fluorescence confocal microscopy setups

Two fluorescence confocal microscopy setups were used for the experiments in this paper: 1) An Olympus IX81 spinning disk confocal microscope, equipped with an Andor FRAPPA photobleach module and Yokogawa CSU-X1 spinning disk. The Andor 400 series solid-state lasers were used to bleach and image the samples. All the images were recorded with a 100× oil immersion objective (numerical aperture 1.5) and an Andor iXon3 EM CCD camera. 2) A Leica SP8 Liachroic-beam splitting confocal laser scanning microscope, equipped with a PMT detector, 2× HyD SP GaAsP detectors, and a Leica DRC7000 GT monochrome camera. All the images recorded using this confocal used an HC PL APO 63×/1.40 (oil) CS2 (0.14 mm) objective.

Two types of microscopy slides were used: 18-well Ibidi chambers for quick imaging, as well as PDMS chambers made in-house. The PDMS chambers were attached onto plasma-primed cover glass slides (no. 1.5H). These PDMS chambers were used for experiments that exceeded 1 h, as Vaseline-sealed coverslips were applied on top to avoid evaporation. For both setups, the glass surfaces were cleaned using a plasma cleaner, then incubated for 1 h with 0.1 mg/mL PLL(2)-g[3.5]-PEG(2) (SuSoS, Dübendorf, Switzerland) dissolved in 10 mM HEPES (pH 8.0) before the surface was thoroughly washed with Milli-Q water and dried with nitrogen gas.

Fluorescence recovery after photobleaching (FRAP)

FRAP experiments were conducted on the Olympus IX81 spinning disk confocal microscope setup. FRAP measurements were carried out by selecting a small region of interest in the middle of a coacervate or aggregate of interest and bleaching with the appropriate wavelength of the laser, depending on the sample. The 488 nm laser line was set at 100% laser power using 75 pulses of 150 μs, and the 647 nm laser line was set to at 100% laser power using 75 pulses of 100 μs. When both wavelengths were used, the 647 nm laser bleaching preceded that of 488 nm laser. The recovery was imaged at reduced laser intensity (at least fivefold lower) and at regular time intervals, depending on the sample.

Using a MATLAB script, the experimental recovery was first normalized before being fitted to a simple exponential, as a first-order approximation of two-dimensional diffusion with a fixed boundary (i.e., droplet edge) (16). Briefly, the exponential decay equation is as follows: $y = A(1 - e^{-bt}) + C$.

From this equation, the recovery half-life (τ) was calculated by $\tau = \ln(2)/b$, and percentage recoveries were extracted by multiplying A by 100. We note that the theoretical maximum recovery is limited by the size of the bleached spot, which was 13.1% ± 4.4% of the droplet area in our experiments, corresponding to a maximum theoretical recovery of ∼87%.

Aging experiments

The CSU temperature stage (Tokai-HIT, Shizuoka, Japan) was used to set the temperature of the samples within a range of 8°C–39°C. Sample temperatures were always confirmed using a thermometer at the end of each experiment. The condensate components and buffers were preincubated at the temperature of interest prior to mixing and were immediately added to functionalized PMDS slides that were sealed with Vaseline. An Arrhenius plot of the τ data revealed two straight lines with a transition around 21°C–22°C (Fig. S2 *A*), and a transistivity plot (Fig. S2 *B*) was derived from the Arrhenius plot to show this drastic transition.

Circularity

The NPM1-rRNA condensates were mixed and deposited onto the Vaseline-sealed PDMS slides incubating at 8°C (sample temperature) (Fig. 2 *C* and *D*). Note that the CSU temperature (Tokai-HIT) stage was set to 4°C, but sample temperature was recorded throughout the experiment using a buffer blank in an adjacent well, and it is the sample temperature that is reported in our figures. Samples were incubated for at least 45 min before imaging began. Sample temperature was adjusted incrementally with a 10 min pause before imaging. At least three different images were captured, and the circularities calculated here were averaged across the population of condensates.

To monitor changes to the condensate circularity upon ATP addition, the NPM1-rRNA condensates were made in 14 mM Mg^{2+} buffer and left to incubate in Ibidi slides for 50 min before 11 mM ATP was added to a corner of the slide. Using the Olympus IX81 confocal microscope, the sample with focus on one large condensate was imaged, and the circularities were calculated over time. We expect the circularity for the single condensate after ATP addition to be less than 1 because the final free Mg^{2+} concentration was 3 mM. Indeed, the circularity of the sample population was 0.85 ± 0.13 after ATP addition.

Raw fluorescence confocal microscopy images and videos were processed and analyzed with MATLAB 2021 Image Processing Toolbox. Objects smaller than 200 pixels were excluded from the analysis (to avoid detecting smaller spherical droplets that tend to initially form as they settle onto the glass), and the area and mean intensity were extracted for every object in each frame. For circularity calculations, the perimeter of each object was calculated by taking the sum of all pixels that were directly adjacent to the dilute phase plus half the sum of all pixels that were only diagonally adjacent to the dilute phase. The circularity (ϑ) of the object cross section was then calculated as $\vartheta = 4\pi A/P^2$, where A is the area of the object and P is the perimeter (17). Subsequently, a single ϑ for each frame was calculated by taking the mean $\vartheta \pm$ standard deviation.

ATP, ADP, and AMP experiments

Samples were prepared in a sequence as outlined above, and nucleotides were mixed last before everything was deposited onto a glass slide for imaging (Fig. 2 *E–G*). The samples were mixed in base buffer containing

14 mM Mg^{2+}, and each nucleotide was at 10 mM final concentration. The FRAP experiments were performed as outlined above. Errors are standard deviations from at least duplicate experiments.

SYBR Gold intensity calculations

SYBR Gold was used to indirectly probe rRNA compaction within the condensates (Fig. S8). According to Kolbeck et al., the SYBR Gold 100,00× stock is 12.4 ± 1.2 mM. Therefore, at 40 nM, the final SYBR Gold concentration used per 30 μL experiment is 62.5× below that of the reported 2.5 μM concentration where quenching effects were observed. SYBR Gold fluorescence is dependent on not just concentration but also local environment (18). To test this, the condensate samples—using unlabeled components—were premixed as outlined above, and the SYBR Gold was added last. In some cases, the Mg^{2+} and ATP were added sequentially after condensate formation. There were no noticeable differences in fluorescence when comparing with premixed and sequential samples. In fact, our reported results are a combination of sequential and premixed intensities.

Since we were comparing SYBR Gold fluorescence between samples with different Mg^{2+} and/or ATP concentrations, the confocal images were taken using the Leica SP8 setup. For all the images, the same laser settings were used. The fluorescence intensity of SYBR Gold from confocal microscopy images and videos were processed and analyzed with MATLAB 2021 Image Processing Toolbox. The images were binarized with an automatic intensity threshold computed with Otsu's method (19). Objects smaller than 50 pixels were excluded from the analysis, and the area and mean intensity were extracted for every object in each frame.

Partitioning experiments

For partitioning of client molecules, we prepared stock solutions at 33 μM 5,6-FAM-RP3 (CASLO, Kongens Lyngby, Denmark) and 50 μM 5,6-FAM-SNORD52 (IDT, Coralville, IA, USA) in the standard base buffer containing 5 mM Mg^{2+}. The ribosome clients, 70S ribosomes-A488 and 70S ribosomes-D650, were thawed and centrifuged for 10 min at 20,000 × *g* to remove any aggregates, and the supernatant was used for partitioning experiments. The ribosome concentration in the supernatants did not diverge much from the stock concentrations described above.

For each partitioning experiment, 1 μL client was mixed with either the forming coacervates or with the RNA component prior to NPM1 addition. Both orders of addition yielded similar results. The mixtures were incubated for 45 min on the glass slides at room temperature, before imaging.

For imaging, we used the Leica confocal setup with laser excitations of 488 nm (FAM, ATTO488) and 647 nm (Dylight650). For each laser setting, a blank was imaged made from NPM1-rRNA with one of the components labeled, accordingly. The partitioning coefficient was then calculated using: $K_p = (I_{coacervate} - I_{background})/(I_{dilute} - I_{background})$, where $I_{coacervate}$ is the average intensity as determined by a pixel gray value cutoff above 40, and I_{dilute} is the average intensity as determined by a pixel gray value cutoff below 10. The errors are standard deviations of at least three sets of K_p values derived from three different images.

Ribosome halo formation

The ribosome halo formation was monitored over time using both confocal setups as highlighted in the video captions. The pixel intensity measurement (Fig. 3 *F*) was from a time-lapse experiment of ATTO488-labeled 70S ribosomes where the video was taken shortly after sample mixing. Using ImageJ, a line of fixed pixel length (equivalent to 9.23 μm) was drawn, and the pixel intensity for each frame of the droplet was measured.

Apyrase enzyme experiments

Apyrase Grade VII from Potato enzyme was dissolved in standard base buffer containing 5 mM Mg^{2+} (20 mM Tris-HCl [pH 7.2], 250 mM potassium glutamate, 5 mM magnesium glutamate). For the FRAP experiment, the samples were made using 5 mM Mg^{2+} base buffer with the following additives: ATP, AMP, and ATP with apyrase. Five U apyrase solution was added to the forming coacervate mix, and all the samples were left to equilibrate on the Ibidi microscope slides for 30 min before imaging and FRAP experiments were performed. Error bars are standard deviations from at least two different photobleaching experiments.

The morphology changes to the NPM1-rRNA condensates were monitored using the Leica SP8 confocal microscope. Again, the samples were prepared as above, with 5 U apyrase added to the forming coacervates. The sample was left to incubate on functionalized Ibidi slides for 30 min prior to imaging using both 488 (NPM1-A488) and 647 nm (rRNA-A647).

Lastly, for the ribosome halo and apyrase experiments, 5 U apyrase solution was added to the formed coacervates on one side of the well of the microscope slide, and the disappearance of the ribosome halo was monitored every 1 s.

RESULTS

Mg^{2+}-induced RNA compaction slows dynamics and leads to gelation

In order to probe the influence of environmental factors on heterotypic condensates that contain both RNA and protein components, we chose NPM1-rRNA as a model system (Fig. 1 *A*). NPM1 proteins are localized to the outer layer of the nucleoli, in the so-called granular component, and were shown to readily form condensates with rRNA *in vitro* (10). Similar to previous work (10), by mixing NPM1 proteins with rRNA in buffer containing no Mg^{2+}, spherical liquid-like droplets appeared. Simultaneous FRAP analyses for both protein and RNA components demonstrated a noticeable difference in FRAP recovery even at 0 mM Mg^{2+} concentration, with a faster recovery half-life (τ) for NPM1 at 18.3 ± 2.4 s and slower recovery for rRNA at 30.7 ± 6.1 s (Fig. 1 *B* and *C*). The τ for NPM1 is comparable to in vivo values of around 20 s (10,20). The difference between protein and RNA recoveries is reminiscent of other intracellular protein-RNA condensates, where the constituent RNAs recover slower than protein components; this was attributed to multivalent RNA-RNA interactions (12,21).

In order to promote such RNA-RNA interactions in the NPM1-rRNA condensates, we increased the Mg^{2+} concentrations and checked the partitioning of each of the components within the condensates (Fig. 1 *D*). At higher Mg^{2+}, rRNA partitions more strongly within condensates. We also observed the NPM1 protein and RNA dynamics diverge, with rRNA recovering slower and to a lesser extent (Fig. 1 *E* and *F*), while NPM1 recovery remained unchanged. At Mg^{2+} concentrations higher than 7 mM, rRNA is fully arrested with $\tau > 1500$ s, and percentage recoveries decreased to $<10\%$ (Fig. 1 *G*). These findings suggest a gradual transition from liquid to an arrested, gel state of the RNA component of the nucleolus, which is supported by the scaling behavior of the relaxation times near the critical point (Fig. 1 *E*) (22,23). The NPM1 component remained astonishingly mobile within the rRNA gel network as the Mg^{2+} concentration increased, with low τ (Fig. 1 *E*), which is consistent with other reported FRAP recoveries for proteins

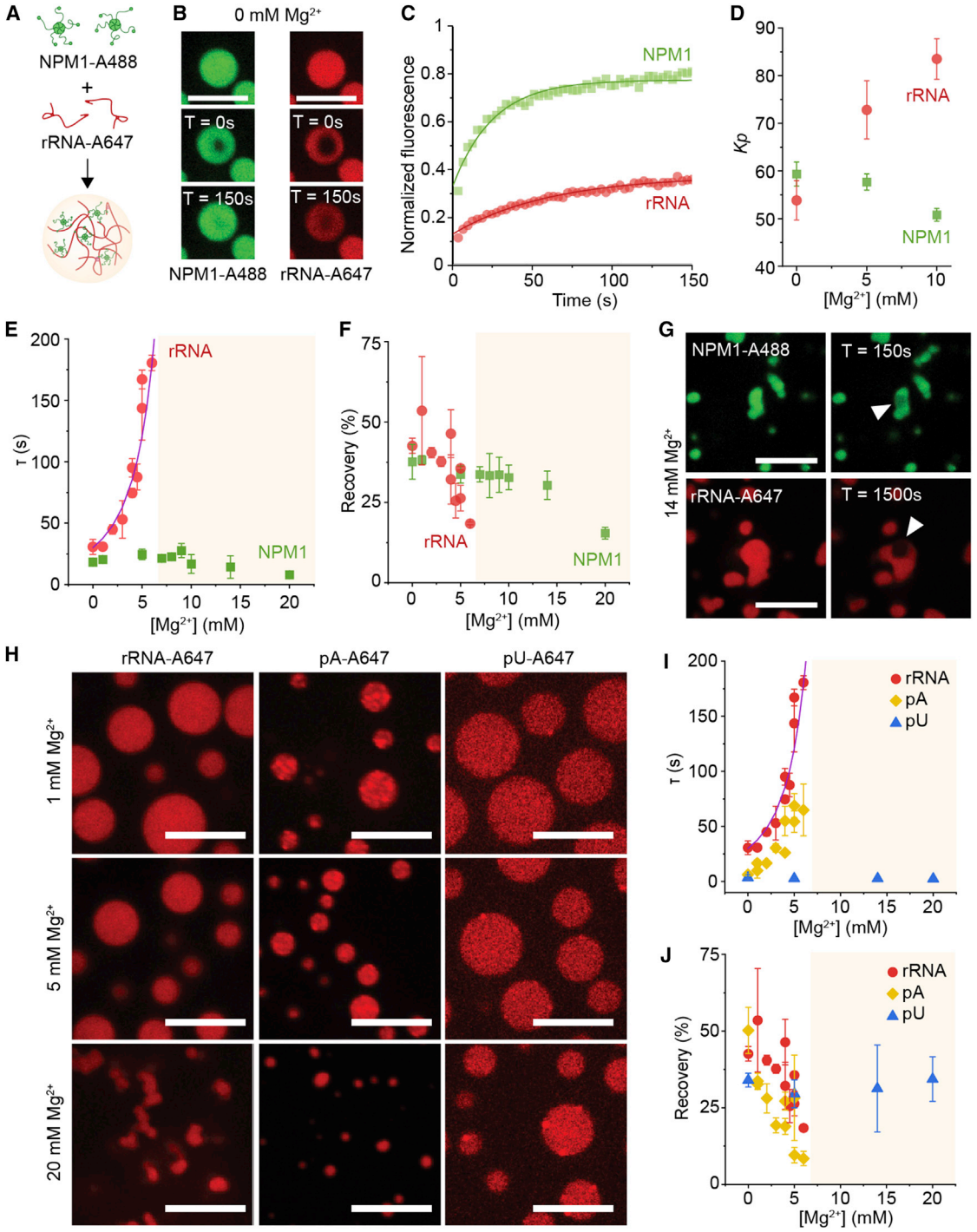

FIGURE 1 Mg^{2+}-induced RNA compaction leads to slow dynamics and gelation. (*A–C*) NPM1 protein and rRNA, both labeled with different fluorophores, are mixed together to form condensates (*A*) that show differences in FRAP recovery (*B* and *C*), where NPM1 (*green*) recovers faster than rRNA (*red*). (*D*) The partitioning coefficients (*Kp*) for NPM1 and rRNA within the condensates at different Mg^{2+} concentrations. (*E*) The recovery of rRNA slows to a halt at Mg^{2+} ion concentrations >7 mM (*shaded in yellow*) and shows critical scaling behavior (*purple fitted line*), indicating that it forms a gel, whereas the NPM1 protein remains mobile. (*F*) The decrease in percentage recovery for both NPM1 and rRNA reflects the gel environment at higher Mg^{2+} concentrations. (*G*) These droplets become gels at higher Mg^{2+} where the rRNA is fully arrested, indicated by bleached regions not recovering (*white arrows*). (*H–J*) In order to test the RNA compaction hypothesis, NPM1-rRNA condensate morphology (*H*) and FRAP recovery parameters (*I* and *J*) were compared with NPM1-pA and NPM1-pU condensates. The errors in this figure are standard deviations from triplicate measurements. Scale bars are all 10 μm.

in tangled RNA networks (10,20). The percentage recovery of NPM1 proteins appeared to not significantly decrease until 20 mM Mg^{2+} was reached (Fig. 1 *F*). NPM1 thus shuttles between different regions of the gelled RNA network. Finally, we note that when rRNA dynamics are fully arrested, the condensates adopt an irregular-shaped morphology (Fig. 1 *G*) with gel-like states that can still slowly fuse together within the timescale of several minutes (Video S1), reminiscent of nucleoli fusing in vivo (9). These results suggest that RNA-RNA interactions, and by extension, Mg^{2+} concentrations, play an important role in shaping condensate dynamics.

Mg^{2+} stabilization of RNA-RNA interactions and corresponding compaction of RNA chains is well reported (1,4,5). The observed rRNA arrest at high Mg^{2+} is likely due to the compaction of RNA, promoted by enhanced RNA-RNA basepairing and -stacking interactions, leading to slowed diffusion of these entangled polymers in the dense phase. To further explore this process, NPM1 condensates were made with other homopolymeric RNAs with different propensities for RNA-RNA interactions. Poly-adenosine (pA) RNA is known to form base-stacking interactions with Mg^{2+}, whereas poly-uridine (pU) remains largely unstructured (24). At 20 mM Mg^{2+}, condensates made from rRNA or pA both formed gels, whereas condensates made from pU remained spherical, liquid droplets (Fig. 1 *H*) that still readily fused with one another within seconds (Video S2). The FRAP parameters also reflected this, with τ increasing for pA at increasing Mg^{2+}, but pU's τs were unaffected by Mg^{2+} (Fig. 1 *I*). The gelation induced by RNA compaction can also be seen in decreasing percentage recoveries for pA at increasing Mg^{2+} concentrations, while pU percentages remained relatively unchanged (Fig. 1 *J*), in agreement with previous studies on Mg^{2+}-induced folding of single 16S rRNA and pU mRNA molecules (25). Together, these results suggest that RNA compaction is facilitated by Mg^{2+}-induced RNA-RNA interactions, which occur in RNAs with strong basepairing and -stacking interactions, such as rRNA and pA, but not in RNAs with weak base-stacking interactions, such as pU. Together, our results suggest that in systems where RNA-RNA interactions can be stabilized with Mg^{2+}, the RNA component imbues protein-RNA condensates with viscoelastic material properties.

Tuning rRNA compaction with temperature and ATP

We hypothesize that RNA forms a viscoelastic network in heterotypic protein-RNA condensates, such as for this NPM1-rRNA system, based indirectly on the partial FRAP recoveries and slowing dynamics with increasing Mg^{2+}. Additional evidence for the viscoelastic nature of the rRNA component is its gradual aging to a more structured state, with slower relaxation observed as an increasing τ over time that reaches a plateau (Fig. 2 *A*). In contrast, the τ of NPM1 remains relatively constant over time (Figs. 2 *B* and S1). This relaxation varies nonlinearly with the inverse temperature ($1/T$), which further supports the viscoelastic nature of rRNA in the condensates. In a pure viscous liquid, where FRAP recovery is commonly attributed to simple Stokes-Einstein diffusion, the diffusion coefficient should increase as $1/T$, and the recovery time should be linearly proportional to temperature. However, this is clearly not the case for NPM1/rRNA condensates as there is a strong nonlinear dependence of τ on T (Fig. 2 *B*). A closer inspection reveals that the temperature dependence shows signs of an activated process that leads to structuring and relaxation. Our data can be fitted using an Arrhenius equation with a fixed activation energy for temperatures above the gel point (Fig. S2 *A*). Below that point, the activation energy increases to a higher level, as shown by the transistivity plot (Fig. S2 *B*), which is characteristic of gels and glasses (26). Therefore, even at 0 mM Mg^{2+}, the rRNA network appears to be a viscoelastic material, held together by multivalent intra- and intermolecular RNA-RNA interactions. In contrast, the NPM1 protein can diffuse freely under all conditions, consistent with observations that nucleoplasmic NPM1 concentrations increase with higher overall NPM1 expression levels (27).

Since Mg^{2+} stabilizes RNA-RNA interactions, it was anticipated that this could affect the τ at maturation of condensates formed in Mg^{2+} buffer. Indeed, condensates made in 5 mM Mg^{2+} had slower observed τ at maturation, which decreased at higher temperature (Fig. S3). This result made us curious about the effect of temperature on Mg^{2+}-stabilized RNA-RNA interactions and how this could impact condensate morphology. NPM1-rRNA condensates formed at 8°C, in either 5 or 10 mM Mg^{2+} buffer after 60 min of incubation, had a striking nonspherical morphology (Figs. 2 *C* and S4). The 10 mM Mg^{2+} condensates appeared smaller and had lower average circularity than the 5 mM Mg^{2+} condensates, but both circularities were lower than at higher temperatures, where values increased closer to 1, which is a characteristic of spherical liquid droplets (17). These results suggest that RNA is fully arrested at lower temperatures in 10 mM Mg^{2+}, with the small gel-like condensates unable to completely fuse together. Instead, the small gel droplets partially fuse, at the time of formation, to form irregular-shaped condensates similar to other gel-like RNA condensates (12). As temperature was increased, the gel-like condensates relaxed and coalesced, eventually, into spherical droplets, which resulted in increased average circularity of the condensate population (Fig. 2 *C*). In fact, the condensates appeared spherical at 35°C, with circularities close to 1, for both Mg^{2+} concentrations. This temperature-dependent relaxation of the NPM1-rRNA condensates manifesting as a morphological change provides further evidence for gelled states being caused by RNA compaction that results in incomplete fusion of gel condensates. Since circularity changes are a one-way process, we demonstrated

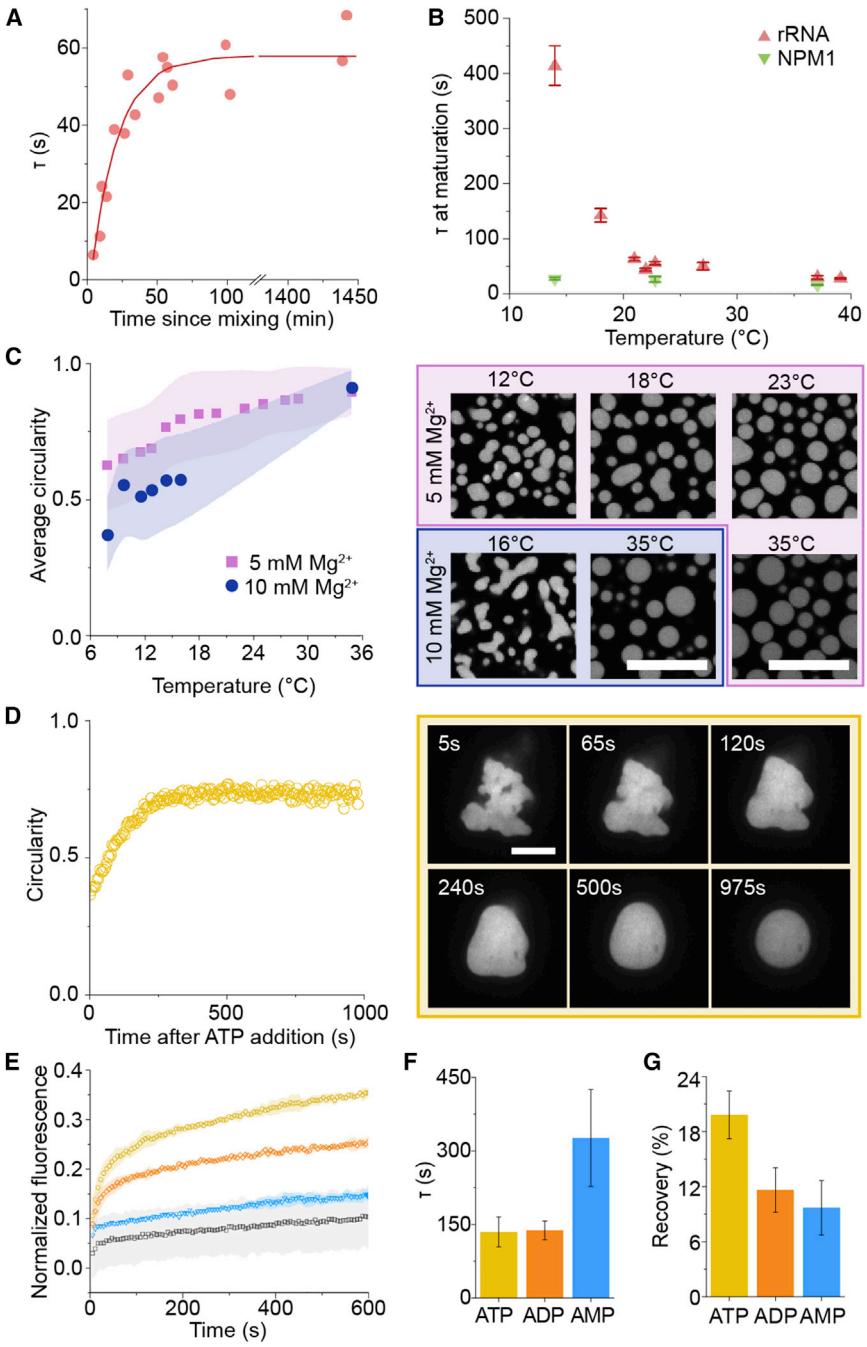

FIGURE 2 Temperature and ATP can reverse the effect of Mg^{2+}-induced RNA condensation. (*A*) NPM1-rRNA condensates aging at 20°C with individual τ for rRNA measured over time (*dots*) and a fitted exponential curve (*line*). (*B*) The extracted plateau τ at maturation for rRNA (*red*) and NPM1 (*green*) was plotted for aged droplets at different temperatures in 0 mM Mg^{2+} buffer. The errors here are derived from the exponential fits. (*C*) Forming NPM1-rRNA condensates at 8°C in buffer containing magnesium resulted in irregular gel-like morphologies that changed to spherical droplets at increasing temperatures, with increased circularities. (*D*) At 20°C, the gels formed in 14 mM Mg^{2+} buffer also liquefied after 11 mM ATP addition, with increasing circularity reflected in the changed morphology of the NPM1-rRNA condensates. (*E*) The FRAP recovery over times for samples that contain ATP (*yellow*), ADP (*orange*), or AMP (*blue*) compared with just the 5 mM Mg^{2+} buffer (*gray*). (*F* and *G*) The extracted τ (*F*) and percentage recoveries (*G*) indicate that the better Mg^{2+}-chelating ability of ATP compared with other adenosine nucleotides caused the condensates to liquefy. The errors in (*E*)–(*G*) are standard deviations from at least duplicate measurements. Scale bars are all 10 μm. To see this figure in color, go online.

thermo-reversibility of the rRNA component in condensates using FRAP (Fig. S5). The responsive morphology changes of NPM1 condensates within the temperature range of living systems hints that this could be an important parameter to consider for nucleoli dynamics.

In homeostatic eukaryotic cells, Mg^{2+} concentrations and temperature are often well regulated (28,29), but local ATP levels are known to fluctuate (7,8). ATP strongly chelates Mg^{2+}, changing the effective free Mg^{2+} concentrations. When we tested the effect of ATP addition to the NPM1-rRNA condensates that were incubated with Mg^{2+}, we observed that ATP caused the gel-like morphologies to liquefy, and the circularity increased over 20 min (Fig. 2 *D*). ATP relaxes the rRNA network, with FRAP recoveries corresponding to the remaining free Mg^{2+} concentrations (Fig. S6). In order to probe the influence of ATP on RNA compaction, we used SYBR Gold fluorescence to probe the RNA-RNA interactions within the condensates. SYBR Gold is a fluorescent dye that intercalates double-stranded nucleic acids (18), and we hypothesize that Mg^{2+} will

stabilize such interactions between the rRNAs. This was indeed the case, as the average SYBR Gold fluorescence detected inside the NPM1-rRNA condensates increased by ~41% on Mg^{2+} addition (Fig. S7). Subsequently, the SYBR Gold fluorescence decreased when ATP was added, providing indirect evidence for decreased RNA compaction due to ATP chelating Mg^{2+} (Fig. S7). This liquefying effect is less pronounced for other adenosine nucleotides (ADP and AMP) that do not chelate Mg^{2+} as effectively (Fig. 2 *E–G*). These results demonstrate how ATP can be a key regulator of free Mg^{2+} concentrations that can impact NPM1-rRNA condensate dynamics.

Consequences of ATP:Mg^{2+} on condensate function: Partitioning of clients

Alongside chelating Mg^{2+}, ATP can also bind to the nucleic acid interacting domain of NPM1 (30,31), which could lead to an altered chemical microenvironment inside the condensates. Inspired by the profound changes to condensate dynamics observed with Mg^{2+} and ATP, we were curious whether these small molecules would influence the partitioning of component proteins, RNAs, and client molecules inside the condensates. Indeed, we observed that at higher Mg^{2+} when there is no ATP, the partitioning coefficient (K_p) of rRNA increased on compaction, and the NPM1 protein K_p decreased, as more RNA-RNA interactions could exclude protein-RNA interactions (Fig. 3 *A* and *B*). ATP increased the K_p of both RNA and protein components. We speculate that ATP, when bound to the nucleic acid interacting domain (30,31), can also stabilize the interaction between NPM1-rRNA because the nucleic acid interacting domain is also where NPM1 binds rRNA (32). As a result, a synergistic increase in partitioning of both components inside the condensates occurred only when Mg^{2+} and ATP were present and not when ADP or AMP were present (Fig. S8).

We then tested whether the altered microenvironment has a functional consequence in the partitioning of two model clients, the $(RRASL)_3$ peptide (RP3) and the SNORD52 RNA. RP3 resembles arginine-rich peptides that can electrostatically interact with both the NPM1 protein and rRNA (33), whereas SNORD52 is a small nucleolar RNA that binds specifically to NPM1 (34) (Fig. 3 *C*). The K_p of both clients followed trends that are expected based on their interaction strengths with the condensate components (Fig. 3 *C*). The SNORD52 RNA K_p increased at higher ATP concentrations as more NPM1 partitioned into the condensates. Conversely, the RP3 K_p decreased as less binding surface was expected due to the synergistic partitioning and interaction of NPM1 and rRNA at higher ATP concentrations. These results indicate that ATP:Mg^{2+} can be used to tune client partitioning within NPM1-rRNA condensates.

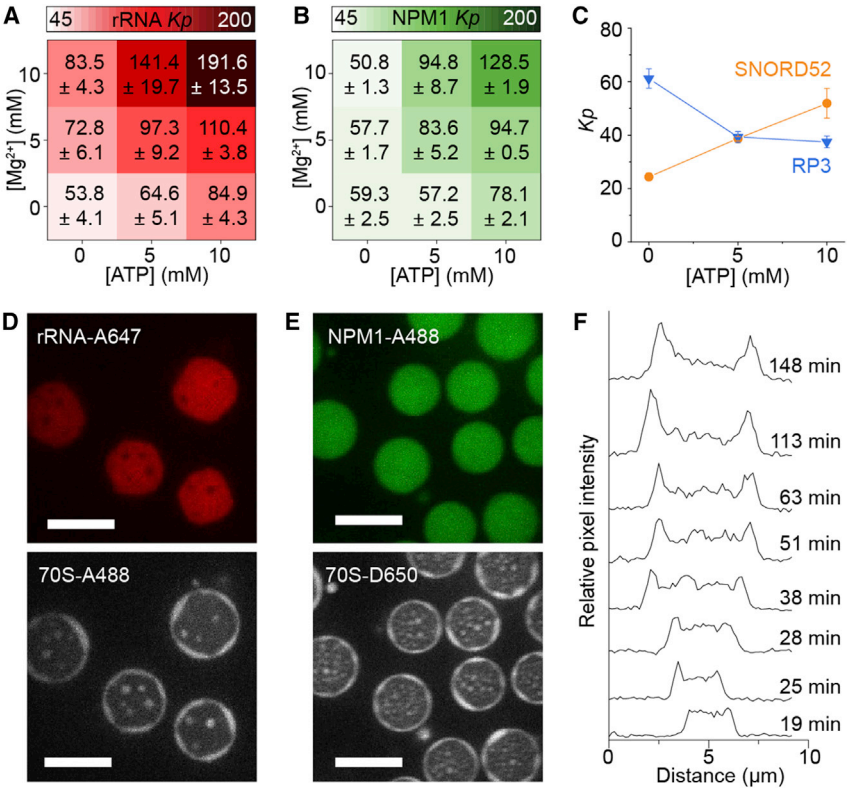

FIGURE 3 The effect of Mg^{2+} and ATP on partitioning of components, clients, and 70S ribosomes. (*A* and *B*) The partitioning coefficients of rRNA (*A*) and NPM1 (*B*) at different Mg^{2+} and ATP concentrations. (*C*) The partitioning coefficients of 5,6-FAM-RP3 peptide (*blue*) and 5,6-FAM-SNORD52 RNA (*orange*) at different ATP concentrations in a 5 mM Mg^{2+} base buffer. (*D* and *E*) Confocal microscope images of NPM1-rRNA condensates with 70S ribosome as the client. The images in (*D*) show that rRNA-A647 is excluded from the ribosome fluorescence, whereas (*E*) shows NPM1-A488 fluorescence as spherical droplets that occupy both locations where there is 70S ribosome and rRNA. (*F*) The formation of the ribosome halo over time as indicated by an increase in fluorescence pixel intensity as peaks at the edges of the droplet. The errors in this figure are standard deviations from triplicate measurements. Scale bars are all 10 μm.

As nucleoli are the sites of ribosome biogenesis, we next investigated the effect of Mg^{2+} and ATP on the partitioning of ribosomes into NPM1-rRNA condensates. Here, we used labeled mature 70S ribosomes that should remain intact at Mg^{2+} concentrations above 5 mM (6). Therefore, it is unsurprising that at increasing Mg^{2+}, the K_p decreased as the ribosomes remained intact in solution (Fig. S9). In contrast, ATP addition resulted in a 30% increase in K_p, likely due to chelation of Mg^{2+} that was previously bound to the ribosomes, thereby destabilizing the ribosome structure and causing it to partition inside the NPM1-rRNA condensate (Fig. S9). This destabilization of ribosome structure was previously reported when free Mg^{2+} concentrations were below 5 mM (35). Interestingly, under conditions where Mg^{2+} concentrations exceeded ATP concentrations, the ribosomes formed a striking halo around the NPM1-rRNA condensates (Fig. 3 *D* and *E*). The ribosome halo excluded the rRNA and resulted in a deformed rRNA condensate shape (Fig. 3 *D*). In contrast, the NPM1 fluorescence is homogeneously distributed throughout the condensates localizing to both the ribosome and rRNA (Fig. 3 *E*), which is expected from a protein that can bind to all rRNAs present. Indeed, these heterotypic multicomponent interactions of NPM1 with rRNA and the preribosomal subunits have been suggested to drive ribosome assembly (27), and here we show that NPM1 bridges the interactions between the rRNA component within the condensates and the 70S ribosomes in the halo.

In order to examine our hypothesis that the halo appeared due to partly destabilized 70S ribosomes, we monitored the condensate growth over time. The ribosome halo appeared after ~25 min, with an increased fluorescence intensity observed around the edge of the condensates (Fig. 3 *F*). Here, the ribosome-NPM1-rRNA condensates exhibited decelerated fusion between larger droplets, in the order of tens of minutes (Video S3). A possible reason for slow droplet fusion could be the viscoelastic nature of the ribosome halo and its rearrangement that would be necessary for rRNA-NPM1 condensates to fuse. Indeed, we found that the ribosome halo had slow FRAP dynamics with an average τ of 490 $\pm$ 10 s and percentage recoveries of 45% $\pm$ 11%. As the droplets fused, the ribosome halo seemed to become incorporated into the condensate and appeared inside as bright spots, with some droplets stalled mid-fusion (Video S3). As a control, we made NPM1-rRNA condensates in 10 mM Mg^{2+} and left these to mature for 2 h, before 5 mM ATP was added, to verify that the observed halo was not a transient phenomenon linked to nucleoli maturation but rather a result of destabilized ribosomes that originate from the dilute phase. Here, the ribosome halo also appeared after approximately ~10 min of ATP addition, alongside separate droplets composed of NPM1 and ribosomes (Videos S4A and S4B; Fig. S10), which is reminiscent of in vivo experiments showing NPM1 interacting with 60S preribosomes (36). Our results suggest that the ATP addition destabilizes the ribosomes in solution, which in turn could liberate ribosome-associated rRNA to interact with NPM1, forming the halo. The exclusion of partially destabilized ribosomes from the NPM1-rRNA condensates is an exciting result as this corroborates the in vivo behavior of nucleoli (27), but to our knowledge, this is the first time this phenomenon has been observed in vitro. Therefore, this work not only provides a useful platform for further studying thermodynamic exclusion from condensates but also suggests that ATP:Mg^{2+} could be one of the ways cells can alter the condensate environment to drive ribosome formation.

Enzymatic depletion of ATP levels changes condensate properties and function

Within cells, ATP levels fluctuate due to a variety of enzymes: from ATP-dependent chaperones to reactions that consume ATP (5,7,8). Here, we demonstrate that ATP removal using a dissipative enzymatic reaction can also control the condensate properties of the nucleolus-like condensates made from NPM1 and rRNA. Using apyrase, an enzyme that converts ATP to AMP (Fig. 4 *A*), we showed that the rRNA recovery of samples without and with apyrase reflected those for the ATP and AMP nucleotides, respectively, similar to observations in Fig. 2 (Fig. 4 *B–D*). Apyrase can effectively liberate Mg^{2+} from ATP, thereby causing rRNA arrest and morphology changes for samples made in high Mg^{2+} concentrations (Fig. 4 *E–G*). This change in morphology from spherical liquid-like to irregular-shaped gel-like states is remarkably similar to observations for purified and in vivo nucleoli when ATP was depleted (9,11). For the purified and in vivo nucleoli, ATP-dependent chaperones were hypothesized to facilitate liquid-like condensate dynamics. However, our results highlight the impact of liberated Mg^{2+} due to ATP depletion and demonstrate that changes to free Mg^{2+} levels may corroborate these in vivo and our in vitro observations. Here, enzymes that consume ATP, and not necessarily active ATP-dependent chaperones, are a possible route that cells use to regulate Mg^{2+} levels and impact nucleoli dynamics.

As nucleoli should exclude fully folded ribosomes (27), we were curious whether ATP removal would affect the previously observed ribosome halo around the NPM1-rRNA condensates. We hypothesized that the ribosome halo was formed from destabilized ribosomes interacting with NPM1, but to what extent the ribosomes were destabilized and whether this was reversible were not yet clear. ATP was depleted using apyrase, which resulted in increased available Mg^{2+} concentrations, and as a result, we observed the striking disappearance of the ribosome halo over time (Fig. 4 *H*). Additionally, the ribosome-NPM1 puncta that formed outside the NPM1-rRNA condensates (Video S5) also vanished on apyrase

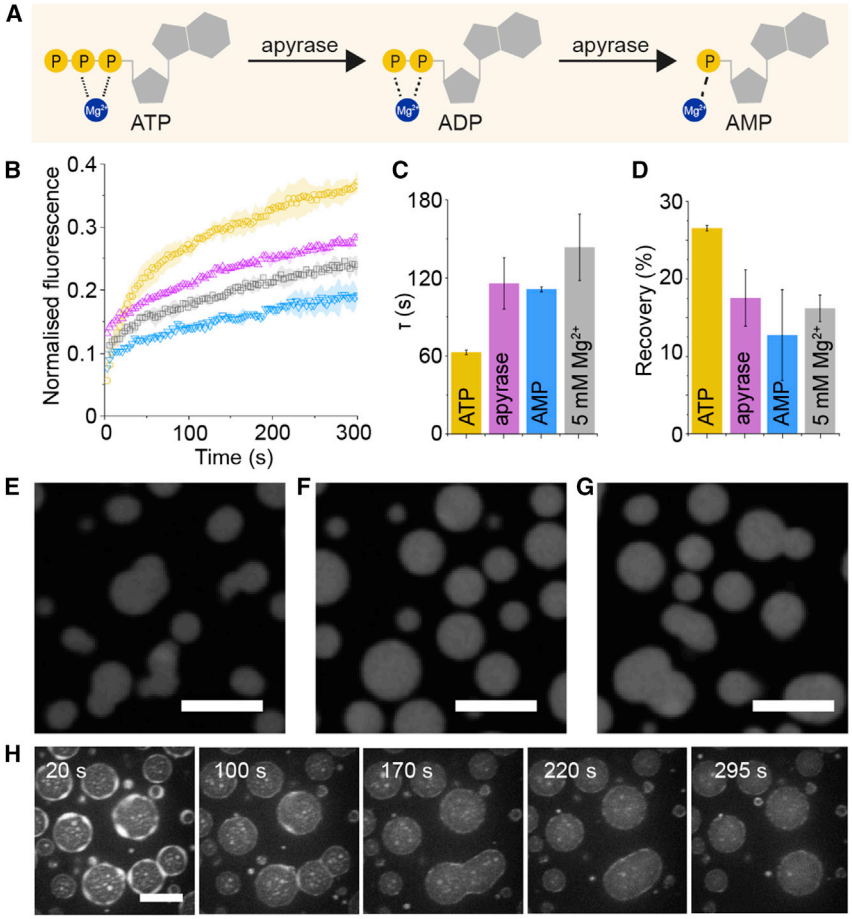

FIGURE 4 Enzymatic control of ATP concentrations influences condensate morphology and dynamics. (*A*) Apyrase enzymes catalyze the removal of phosphate groups from ATP to form AMP, a nucleotide that poorly chelates Mg^{2+}. (*B–D*) The effect of apyrase on the dynamics of rRNA after FRAP is clearly shown, where rRNA recovery in the presence of ATP (*yellow*) drops when apyrase (*purple*) is added. (*C* and *D*) In fact, the resulting FRAP parameters show that apyrase converts ATP to AMP, which imbues the rRNA with gel-like dynamics, similar to condensates made in 5 mM Mg^{2+} buffer (*grey*). (*E–G*) The morphology of NPM1-rRNA condensates at 18°C in 5 mM Mg^{2+} buffer (*E*) with 5 mM ATP added (*F*) and when apyrase is also added (*G*) shows the changes in morphology that is expected from gel-like condensates in buffer containing Mg^{2+} that stabilizes RNA-RNA interactions and spherical morphology in conditions where ATP chelates the Mg^{2+} and liquefies these interactions. (*H*) This series of confocal images over time of labeled 70S ribosomes shows the disappearance of the ribosome halo and puncta as apyrase was added. ATP depletion results in higher Mg^{2+}, which stabilizes the ribosomes and causes them to dissipate back into the dilute phase. The errors in this figure are standard deviations from triplicate measurements. Scale bars are all 10 μm. To see this figure in color, go online.

addition, suggesting that fully folded ribosomes are excluded from the NPM1-rRNA condensates. With the disappearance of the ribosome halo, the NPM1-rRNA condensates that were previously stabilized mid-fusion were able to relax and fuse again, and the resulting condensates appeared unexpectedly spherical in shape (Video S6), despite the higher available Mg^{2+} concentrations. The more spherical final condensates are hypothesized to be a result of altered Mg^{2+} ions concentrations: although liberated from ATP, the Mg^{2+} will likely bind to the 70S ribosomes, making the ion less available to stabilize rRNA-rRNA interactions. These results demonstrate that enzymatic changes to ATP concentrations can have a profound effect on client localization around the NPM1-rRNA condensates and could indeed be a way how cells change the flux of client molecules interacting with nucleoli.

DISCUSSION

Many biomolecular condensates are portrayed as heterotypic protein-RNA droplets with viscoelastic material properties, governed primarily by interactions between proteins and RNA (2,3,37,38). However, here we show that the RNA component itself has a determining role in the shape, dynamics, and material properties of protein-RNA condensates, especially in systems where the RNA network is formed via RNA-RNA interactions tunable by changes in ATP:Mg^{2+} or temperature. The viscoelastic properties of the RNA network depend on the structure of the RNA and the strengths of the intermolecular RNA-RNA interactions. NPM1-pU condensates, for example, remained largely liquid like even at high Mg^{2+}, suggesting that pU RNAs do not form a strong network, while NPM1-rRNA and NPM1-pA condensates showed dynamic arrest at high Mg^{2+}. Indeed, our results at high Mg^{2+} for rRNA and pA condensates are reminiscent of the gel-like morphologies observed in reconstituted protein-RNA condensates, where increased intermolecular interactions are engineered for one component, either protein (39) or RNA (12,24), within the network. Here, we demonstrate that also the environment can influence the intermolecular interactions in RNA, and this can be a way to control the dynamic material properties of protein-RNA condensates, like NPM1-rRNA condensates.

Homotypic protein-based condensates were previously shown to mature over time as viscoelastic Maxwell fluids

(40), with slowed aging at increased temperatures. The aging of NPM1-rRNA condensates is similarly temperature dependent with faster τ at maturation for RNA at higher temperatures. This plateau in τ observed after 1 h is also reminiscent of another in vitro system of protein-only condensates formed via Ni^{2+} interactions (41). Additionally, an aging phenomenon was also documented for in vivo protein-RNA condensates where FRAP recoveries of the protein component at 5 h after formation was faster than at 16 h (12). Although the physiological relevance is still unknown, aging seems to be a common feature of viscoelastic condensates formed via multivalent interactions, and here, we show for the first time that the RNA component also undergoes aging.

Since nucleoli are rich in RNA (42), our work on NPM1-rRNA condensates, highlighting the considerable influence of ATP:Mg^{2+} on the dynamics of the RNA network, can in turn help us better interpret the puzzling observations of actual nucleoli. Indeed, in vivo nucleoli are gel like, with slow fusion timescales of ~30 min and nonspherical shapes (9–11); however, the localized proteins had fast dynamics, in the order of seconds (20,43), which never explained the material properties of nucleoli. By considering the RNA component, our work shows that NPM1-rRNA condensates at 5 mM Mg^{2+} fused in the order of minutes (Video S1), and at Mg^{2+} concentrations >7 mM, gel-like morphologies were observed. Our reconstituted system approximates nucleoli and, along with recent findings of rRNA movement through the nucleolus (44), supports this hypothesis that the viscoelastic contribution of RNA in nucleoli accounts for its irregular shapes and slow fusion dynamics.

Additionally, our in vitro studies provide a valuable caveat for the interpretation of underlying causes observed in ATP depletion studies. Numerous works on ATP-depleted nucleoli, purified and in vivo, resulted in irregularly shaped structures reminiscent of incomplete fusion (9,11,45,46), and a similar observation of slowed recovery dynamics was observed in ATP-depleted cells containing CAG-repeat RNA condensates (47). The slowed condensate dynamics upon ATP depletion in all cases was attributed to an unknown ATP-dependent process/enzyme required to maintain condensate fluidity. However, our ATP-depleted in vitro model, when apyrase was added, challenges this perspective. Here, the depleted ATP liberates Mg^{2+}, resulting in the morphed gel-like appearance of the protein-RNA condensates. Our results can help explain these in vivo observations, without the need for ATP-dependent enzymatic activity to maintain condensate fluidity, by highlighting the importance of considering free Mg^{2+} in the interpretation of ATP depletion results. Beyond enzymes, it is also valuable to consider the changes in ATP levels during a cell cycle (8,48) and how this could impact the fluidity and condensate properties of nucleoli and other protein-RNA condensates.

Together, our results show that protein-RNA condensates are responsive, responding to changes in the local environment from temperature to differences in Mg^{2+} and ATP concentrations. The small molecules influenced partitioning of constituent condensate components, which in turn affected client partitioning. Transient changes to ATP levels may be how cells regulate the amount of free Mg^{2+} and thereby control the dynamics of RNA-based condensates, such as the nucleolus.

SUPPORTING MATERIAL

Supporting material can be found online at https://doi.org/10.1016/j.bpj.2022.08.025.

AUTHOR CONTRIBUTIONS

N.A.Y. and E.S. generated the ideas and wrote the paper with helpful suggestions of all the authors. N.A.Y. performed the experiments and analyzed the data. A.A.M.A. assisted in protein and rRNA preparation. MHIvH wrote the MATLAB scripts. F.H.T.N. and A.J. prepared the ribosomes.

ACKNOWLEDGMENTS

We thank Prof. Richard Kriwacki (St. Jude Children's Hospital) for providing us with the NPM1-GFP plasmid and Davin Elian for his help in cloning the NPM1-WT plasmid. Lastly, we thank Dr. Aigars Piruska (Radboud University) for his assiduous patience and microscopy technician skills. This work was supported by the Netherlands Organisation for Scientific Research (NWO) through a Startup grant to E.S.

DECLARATION OF INTERESTS

The authors have no conflict of interest.

REFERENCES

1. Roden, C., and A. S. Gladfelter. 2021. RNA contributions to the form and function of biomolecular condensates. *Nat. Rev. Mol. Cell Biol.* 22:183–195. https://doi.org/10.1038/s41580-020-0264-6.
2. Guo, L., and J. Shorter. 2015. It's raining liquids: RNA tunes Viscoelasticity and dynamics of membraneless organelles. *Mol. Cell.* 60:189–192. https://doi.org/10.1016/j.molcel.2015.10.006.
3. Rhine, K., V. Vidaurre, and S. Myong. 2020. RNA droplets. *Annu. Rev. Biophys.* 49:247–265. https://doi.org/10.1146/annurev-biophys-052118-115508.
4. Yamagami, R., J. P. Sieg, and P. C. Bevilacqua. 2021. Functional roles of chelated magnesium ions in RNA folding and function. *Biochemistry.* 60:2374–2386. https://doi.org/10.1021/acs.biochem.1c00012.
5. Wright, R. H. G., F. Le Dily, and M. Beato. 2019. ATP, Mg^{2+}, nuclear phase separation, and genome accessibility. *Trends Biochem. Sci.* 44:565–574. https://doi.org/10.1016/j.tibs.2019.03.001.
6. Nierhaus, K. H. 2014. Mg^{2+}, K^{+}, and the ribosome. *J. Bacteriol.* 196:3817–3819. https://doi.org/10.1128/JB.02297-14.
7. Gout, E., F. Rébeillé, R. Bligny…, 2014. Interplay of Mg^{2+}, ADP, and ATP in the cytosol and mitochondria: unravelling the role of Mg^{2+} in cell respiration. *Proc. Natl. Acad. Sci. USA.* 111:E4560–E4567. https://doi.org/10.1073/pnas.1406251111.

8. Maeshima, K., T. Matsuda, T. Nagai…, 2018. A transient rise in free Mg^{2+} ions released from ATP-Mg hydrolysis contributes to mitotic chromosome condensation. *Curr. Biol.* 28:444–451.e6. https://doi.org/10.1016/j.cub.2017.12.035.
9. Brangwynne, C. P., T. J. Mitchison, and A. A. Hyman. 2011. Active liquid-like behavior of nucleoli determines their size and shape in Xenopus laevis oocytes. *Proc. Natl. Acad. Sci. USA.* 108:4334–4339. https://doi.org/10.1073/pnas.1017150108.
10. Feric, M., N. Vaidya, C. P. Brangwynne…, 2016. Coexisting liquid phases underlie nucleolar subcompartments. *Cell.* 165:1686–1697. https://doi.org/10.1016/j.cell.2016.04.047.
11. Caragine, C. M., S. C. Haley, and A. Zidovska. 2019. Nucleolar dynamics and interactions with nucleoplasm in living cells. *Elife.* 8:e47533. https://doi.org/10.7554/eLife.47533.
12. Ma, W., G. Zheng, …, C. Mayr. 2021. In vivo reconstitution finds multivalent RNA–RNA interactions as drivers of mesh-like condensates. *Elife.* 10:e64252. https://doi.org/10.7554/eLife.64252.
13. Mitrea, D. M., J. A. Cika, R. W. Kriwacki…, 2016. Nucleophosmin integrates within the nucleolus via multi-modal interactions with proteins displaying R-rich linear motifs and rRNA. *Elife.* 5:e13571. https://doi.org/10.7554/eLife.13571.
14. Vibhute, M. A., M. H. Schaap, W. T. S. Huck…, 2020. Transcription and translation in cytomimetic protocells perform most efficiently at distinct macromolecular crowding conditions. *ACS Synth. Biol.* 9:2797–2807. https://doi.org/10.1021/acssynbio.0c00330.
15. Awwad, D. A., A. R. Rahmouni, and F. Aboul-Ela. 2020. Protocol for efficient fluorescence 3' end-labeling of native noncoding RNA domains. *MethodsX.* 7:101148. https://doi.org/10.1016/j.mex.2020.101148.
16. Taylor, N. O., M. T. Wei, C. P. Brangwynne…, 2019. Quantifying dynamics in phase-separated condensates using fluorescence recovery after photobleaching. *Biophys. J.* 117:1285–1300. https://doi.org/10.1016/j.bpj.2019.08.030.
17. Spoelstra, W. K., E. O. van der Sluis, L. Reese…, 2020. Nonspherical coacervate shapes in an enzyme-driven active system. *Langmuir.* 36:1956–1964. https://doi.org/10.1021/acs.langmuir.9b02719.
18. Kolbeck, P. J., W. Vanderlinden, …, J. Lipfert. 2021. Molecular structure, DNA binding mode, photophysical properties and recommendations for use of SYBR Gold. *Nucleic Acids Res.* 49:5143–5158. https://doi.org/10.1093/nar/gkab265.
19. Otsu, N. 1979. A threshold selection method from gray-level histograms. *IEEE Trans. Syst. Man Cybern.* 9:62–66. https://doi.org/10.1109/tsmc.1979.4310076.
20. Negi, S. S., and M. O. J. Olson. 2006. Effects of interphase and mitotic phosphorylation on the mobility and location of nucleolar protein B23. *J. Cell Sci.* 119:3676–3685. https://doi.org/10.1242/jcs.03090.
21. Guillén-Boixet, J., A. Kopach, and T. M. Franzmann. 2020. RNA-induced conformational switching and clustering of G3BP drive stress granule assembly by condensation. *Cell.* 181:346–361.e17. https://doi.org/10.1016/j.cell.2020.03.049.
22. Mours, M., and H. H. Winter. 1996. Relaxation patterns of nearly critical gels. *Macromolecules.* 29:7221–7229.
23. Suman, K., and Y. M. Joshi. 2020. On the universality of the scaling relations during sol-gel transition. *J. Rheol.* 64:863–877. https://doi.org/10.1122/1.5134115.
24. Boeynaems, S., A. S. Holehouse, …, A. D. Gitler. 2019. Spontaneous driving forces give rise to protein−RNA condensates with coexisting phases and complex material properties. *Proc. Natl. Acad. Sci. USA.* 116:7889–7898. https://doi.org/10.1073/pnas.1821038116.
25. Newby Lambert, M., E. Vöcker, N. G. Walter…, 2006. Mg^{2+}-induced compaction of single RNA molecules monitored by tethered particle microscopy. *Biophys. J.* 90:3672–3685. https://doi.org/10.1529/biophysj.105.067793.
26. Carvalho-Silva, V. H., N. D. Coutinho, and V. Aquilanti. 2019. Temperature dependence of rate processes beyond Arrhenius and eyring: activation and transitivity. *Front. Chem.* 7:380. https://doi.org/10.3389/fchem.2019.00380.
27. Riback, J. A., L. Zhu, C. P. Brangwynne…, 2020. Composition-dependent thermodynamics of intracellular phase separation. *Nature.* 581:209–214. https://doi.org/10.1038/s41586-020-2256-2.
28. Gabriel, T. E., and D. Günzel. 2007. Quantification of Mg^{2+} extrusion and cytosolic Mg^{2+}-buffering in Xenopus oocytes. *Arch. Biochem. Biophys.* 458:3–15. https://doi.org/10.1016/j.abb.2006.07.007.
29. Romani, A. M. P. 2011. Intracellular magnesium homeostasis. *In* Magnesium in the Central Nervous System, pp. 13–58.
30. Chang, J. H., J. Y. Lin, B. Y. Yung…, 1998. Evidence for the ability of nucleophosmin/B23 to bind ATP. *Biochem. J.* 329:539–544. https://doi.org/10.1042/bj3290539.
31. Choi, J. W., S. B. Lee, …, K. H. Lee. 2008. Disruption of ATP binding destabilizes NPM/B23 and inhibits anti-apoptotic function. *BMB Rep.* 41:840–845. https://doi.org/10.5483/bmbrep.2008.41.12.840.
32. Wang, D., A. Baumann, …, M. O. Olson. 1994. The nucleic acid binding activity of nucleolar protein B23.1 resides in its carboxyl-terminal end. *J. Biol. Chem.* 269:30994–30998. https://doi.org/10.1016/S0021-9258(18)47380-2.
33. Musinova, Y. R., E. Y. Kananykhina, E. V. Sheval…, 2015. A charge-dependent mechanism is responsible for the dynamic accumulation of proteins inside nucleoli. *Biochim. Biophys. Acta.* 1853:101–110. https://doi.org/10.1016/j.bbamcr.2014.10.007.
34. Nachmani, D., A. H. Bothmer, P. P. Pandolfi…, 2019. Germline NPM1 mutations lead to altered rRNA 2'-O-methylation and cause dyskeratosis congenita. *Nat. Genet.* 51:1518–1529. https://doi.org/10.1038/s41588-019-0502-z.
35. Yamamoto, T., Y. Shimizu, Y. Shiro…, 2010. Mg^{2+} dependence of 70 S ribosomal protein flexibility revealed by hydrogen/deuterium exchange and mass spectrometry. *J. Biol. Chem.* 285:5646–5652. https://doi.org/10.1074/jbc.M109.081836.
36. Okuwaki, M., S. Saito, K. Nagata…, 2021. The interaction between nucleophosmin/NPM1 and the large ribosomal subunit precursors contribute to maintaining the nucleolar structure. *Biochim. Biophys. Acta Mol. Cell Res.* 1868:118879. https://doi.org/10.1016/j.bbamcr.2020.118879.
37. Alshareedah, I., G. M. Thurston, and P. R. Banerjee. 2021. Quantifying viscosity and surface tension of multicomponent protein-nucleic acid condensates. *Biophys. J.* 120:1161–1169. https://doi.org/10.1016/j.bpj.2021.01.005.
38. Iglesias-Artola, J. M., B. Drobot, …, M. Kreysing. 2022. Charge-density reduction promotes ribozyme activity in RNA–peptide coacervates via RNA fluidization and magnesium partitioning. *Nat. Chem.* 14:407–416. https://doi.org/10.1038/s41557-022-00890-8.
39. Zhu, L., T. M. Richardson, C. P. Brangwynne…, 2019. Controlling the material properties and rRNA processing function of the nucleolus using light. *Proc. Natl. Acad. Sci. USA.* 116:17330–17335. https://doi.org/10.1073/pnas.1903870116.
40. Jawerth, L., E. Fischer-Friedrich, F. Jülicher…, 2020. Protein condensates as aging Maxwell fluids. *Science.* 370:1317–1323. https://doi.org/10.1126/science.aaw4951.
41. Hong, K., D. Song, and Y. Jung. 2020. Behavior control of membraneless protein liquid condensates with metal ion-induced phase separation. *Nat. Commun.* 11:5554. https://doi.org/10.1038/s41467-020-19391-8.
42. Latonen, L. 2019. Phase-to-phase with nucleoli - stress responses, protein aggregation and novel roles of RNA. *Front. Cell. Neurosci.* 13:151. https://doi.org/10.3389/fncel.2019.00151.
43. Okuwaki, M., A. Sumi, K. Nagata…, 2012. Function of homo- and hetero-oligomers of human nucleoplasmin/nucleophosmin family proteins NPM1, NPM2 and NPM3 during sperm chromatin remodeling. *Nucleic Acids Res.* 40:4861–4878. https://doi.org/10.1093/nar/gks162.
44. Riback, J. A., J. M. Eeftens, D. S. W. Lee, S. A. Quinodoz, L. Beckers, L. A. Becker…, 2022. Viscoelastic RNA entanglement and advective flow underlies nucleolar form and function. *Preprint at bioRxiv.* https://doi.org/10.1101/2021.12.31.474660.

45. Hayes, M. H., E. H. Peuchen, …, D. L. Weeks. 2018. Dual roles for ATP in the regulation of phase separated protein aggregates in Xenopus oocyte nucleoli. *Elife.* 7:e35224. https://doi.org/10.7554/eLife.35224.

46. Park, H., S. S. Han, …, C. G. Pack. 2015. Dynamic and unique nucleolar microenvironment revealed by fluorescence correlation spectroscopy. *FASEB J.* 29:837–848. https://doi.org/10.1096/fj.14-254110.

47. Jain, A., and R. D. Vale. 2017. RNA phase transitions in repeat expansion disorders. *Nature.* 546:243–247. https://doi.org/10.1038/nature22386.

48. Kang, J. H., G. Katsikis, …, T. P. Miettinen. 2020. Monitoring and modeling of lymphocytic leukemia cell bioenergetics reveals decreased ATP synthesis during cell division. *Nat. Commun.* 11:4983. https://doi.org/10.1038/s41467-020-18769-y.